Chen, Guangze; Lado, Jose; Song, Fei

Many-body Liouvillian dynamics with a non-Hermitian tensor-network kernel polynomial algorithm

Many-body Liouvillian dynamics with a non-Hermitian tensor-network kernel polynomial algorithm

Guangze Chen [1] Jose L. Lado [2] and Fei Song [3,*]

[1]*Department of Microtechnology and Nanoscience, Chalmers University of Technology, 41296 Göteborg, Sweden*
[2]*Department of Applied Physics, Aalto University, 02150 Espoo, Finland*
[3]*Kavli Institute for Theoretical Sciences, Chinese Academy of Sciences, Beijing 100190, China*

Understanding the dynamics of open quantum many-body systems is a major problem in quantum matter. Specifically, efficiently solving the spectrum of the Liouvillian superoperator governing such dynamics remains a critical open challenge. Here, we put forward a method for solving the many-body Liouvillian spectrum and dynamics based on the non-Hermitian kernel polynomial method and tensor-network techniques. We demonstrate the faithfulness of our method by computing the dynamics of the dephasing quantum compass model with a gradient magnetic field and comparing it with exact results. In particular, we show that our method allows us to characterize the quantum Zeno crossover and the reduction of relaxation rate due to Stark localization in this model. We further demonstrate the ability of our method to go beyond exact results by exploring nearest-neighbor interaction effects on the Liouvillian dynamics, elucidating the interplay between Stark localization and many-body interactions. Our method provides an efficient solution to many-body Liouvillian spectrum and dynamics, establishing a methodology to explore large open quantum many-body systems.

I. INTRODUCTION

Exploring quantum dynamics provides a versatile approach to characterize both closed and open quantum systems [1,2]. Unlike the coherent dynamics in closed systems, which is solely generated by the Hamiltonian, open quantum dynamics is subject to both quantum coherence and dissipative effects. The interplay between coherent and dissipative dynamics can motivate open quantum systems to approach nonequilibrium steady states with exotic properties after a long-time evolution [3–7]. Moreover, beyond steady states, the open quantum dynamics shares deep connections with a variety of areas in quantum physics, including many-body physics [8–13], random matrix theory [14,15], and non-Hermitian quantum mechanics [16–21].

Under the Markovian assumption, the dynamics of an open quantum system follows the Lindblad master equation that is generated by a Liouvillian superoperator [22,23]. Plenty of information can be extracted from the spectrum of the Liouvillian, such as the non-Hermitian topology that links to the presence of the Liouvillian skin effect [16–18,24], and the complex level statistics as a criterion of the quantum chaos in open quantum systems [25–27]. Nevertheless, except for several specific models [28–31], it is often very challenging to

exactly solve the Liouvillian spectrum in many-body systems [32]. Thus, efficient numerical methods are needed.

Here, we put forward a methodology to compute dynamical correlators of the Liouvillian superoperator, that provide access to the Liouvillian spectrum and the Liouvillian dynamics, by combining the non-Hermitian kernel polynomial method (NHKPM) [33] with tensor-network-based techniques [34]. The NHKPM is a generalization of the Kernel polynomial method [35], an efficient method to compute dynamical correlators in Hermitian systems [36,37], to non-Hermitian cases. It relies on expanding the correlator into Chebyshev polynomials and recursively calculating the expansion coefficients. Due to the simple mathematical structure of the recursion relations, the NHKPM can be efficiently implemented with matrix-product states (MPS), making it suitable for many-body calculations with low-entangled states. For many-body Liouvillians, we find that, with a proper vectorization [38] of the density-matrix such that it becomes a low-entangled state while transforming the Liouvillian into a non-Hermitian model with only short-range interactions, the NHKPM implemented with MPS can efficiently solve the Liouvillian spectrum.

We demonstrate our methodology with the dephasing quantum compass model [29] with a gradient magnetic field, known to reduce the relaxation rate of unequal-time correlations of spins due to Stark localization [39–42]. We first benchmark our method with exact results in small systems, where we demonstrate that our method faithfully computes the Liouvillian dynamics. This allows us to characterize quantum Zeno crossovers [31,43] and Stark localization effects in the dynamics. Furthermore, to eliminate finite-size effects that hinder Stark localization at small magnetic field gradients, we consider a large system size, where the faithfulness of

---

*Contact author: songfeiphys@gmail.com

our method is demonstrated based on the closed hierarchy of correlations [44,45]. Finally, moving beyond the capability of exact methods, we show that our method can be applied to explore the influence of nearest-neighbor interactions on the Liouvillian dynamics.

II. MODEL AND METHOD

We consider the Liouvillian

$$\mathcal{L}[\rho] = -i[H, \rho] + \sum_l \left(L_l \rho L_l^\dagger - \frac{1}{2} \{ L_l^\dagger L_l, \rho \} \right) \quad (1)$$

with the following Hamiltonian:

$$H = -\sum_{l=1}^{N/2} J_x \sigma_{2l-1}^x \sigma_{2l}^x - \sum_{l=1}^{N/2-1} J_y \sigma_{2l}^y \sigma_{2l+1}^y + \sum_{l=1}^{N} B(l-1)\sigma_l^z, \quad (2)$$

and Lindblad dissipators $L_l = \sqrt{\gamma}\sigma_l^z$, where l is the site index and B is a gradient magnetic field [Fig. 1(a)]. The Lindblad dissipators describe the process of dephasing, which can originate from density-density coupling to a bath with infinite temperature such as a Floquet system [46], or from successive measurements of σ_i^z [47]. When the gradient magnetic field vanishes, i.e., $B = 0$, this model reduces to the solvable quantum compass model with dephasing [29], which is known to host a quantum Zeno crossover [31,43]: when γ is small, the long-time relaxation rate of an initial state increases with γ, whereas when γ is large, the long-time relaxation rate decreases with γ. On the other hand, a finite B is known to lead the Hamiltonian to exhibit Stark localization in both single-particle and many-body cases [39,40], while it also destroys the solvability of the Liouvillian. The main object in the following is thus to introduce an efficient numerical method that uncovers the effect of Stark localization on Liouvillian dynamics.

Using dynamical correlators of the Liouvillian, we show the reduction of the relaxation rate with increasing B for our model. In particular, we consider the relaxation of σ_N^z above the steady state, which can be characterized by the following autocorrelator:

$$C(t) = \text{tr}(\sigma_N^z(t)\sigma_N^z(0)\rho_s) = \text{tr}(\sigma_N^z e^{t\mathcal{L}}[\sigma_N^z \rho_s]), \quad (3)$$

where ρ_s is the density matrix of the steady state. Since our model only possesses Hermitian dissipators and conserves the parity operator $Q = \prod_{l=1}^{N} \sigma_l^z$, it has two degenerate steady states $\rho_\pm = (\mathbf{I} \pm Q)/2^N$ where $\mathbf{I}$ denotes the identity matrix in the Pauli basis. Note that our method is applicable as long as ρ_s is a low-entangled state after proper vectorization. We choose $\rho_s = (\rho_+ + \rho_-)/2 = \mathbf{I}/2^N$ that fulfills this requirement in the following calculations [48].

To compute the correlator Eq. (3), we vectorize a density matrix ρ as

$$\rho = \sum_{\sigma_1 \cdots \sigma_N} \sum_{\tau_1 \cdots \tau_N} \rho_{\sigma_1 \cdots \sigma_N \tau_1 \cdots \tau_N} |\sigma_1 \cdots \sigma_N\rangle\langle\tau_1 \cdots \tau_N|$$

$$\rightarrow |\tilde{\rho}\rangle = \sum_{\sigma_1 \cdots \sigma_N} \sum_{\tau_1 \cdots \tau_N} \rho_{P[\sigma_1 \cdots \sigma_N \tau_1 \cdots \tau_N]} |\sigma_1 \cdots \sigma_N\rangle|\tau_1 \cdots \tau_N\rangle, \quad (4)$$

where $\tau_1 \cdots \tau_N$ are the degrees of freedom of the left vector in ρ, and $P[\tau_l] = \sigma_{2l}$, $P[\sigma_l] = \sigma_{2l-1}$ is a permutation of
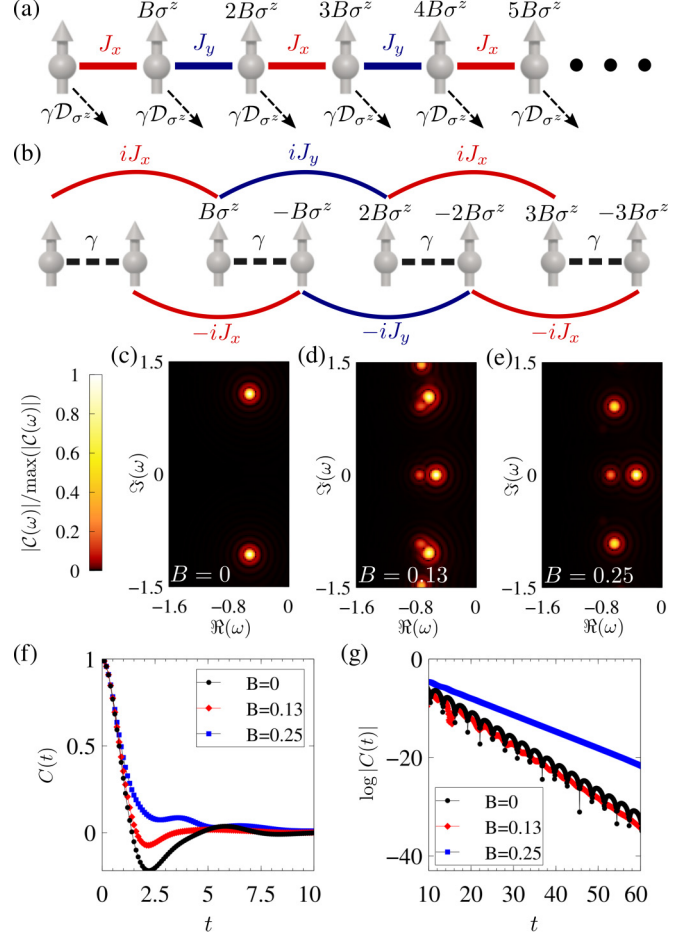

FIG. 1. The Liouvillian model and its dynamics. (a) The model Liouvillian Eq. (1) with N spins, where $\mathcal{D}$ is the Lindblad dissipator [second term in Eq. (1)]. (b) The Liouvillian can be transformed into the non-Hermitian spin model Eq. (5). (c)–(e) The dynamical correlator of the Liouvillian $\mathcal{C}(\omega)$ in Eq. (8) computed with $N = 4$, $J_x = 0.75$, $J_y = 0.5$, $\gamma = 0.2$ and different magnetic field gradients $B = 0$, 0.13, and 0.25. (f), (g) The autocorrelator $C(t)$ in Eq. (6) computed with parameters in panels (c)–(e), showing the short and long-time dynamics. The long-time dynamics highlights the similar relaxation rates for $B = 0$ and $B = 0.13$, and a smaller relaxation rate for $B = 0.25$.

spin degrees of freedom on different sites. The advantage of implementing the permutation P is that the transformed Liouvillian $\tilde{\mathcal{L}}$, which satisfies $\tilde{\mathcal{L}}|\tilde{\rho}\rangle = |\widetilde{\mathcal{L}[\rho]}\rangle$, will become a non-Hermitian spin model with only nearest and next-nearest neighbor interactions (see details in Appendix A) [Fig. 1(b)]:

$$\tilde{\mathcal{L}} = iJ_x \sum_{l=1}^{N/2} \left(\sigma_{4l-3}^x \sigma_{4l-1}^x - \sigma_{4l-2}^x \sigma_{4l}^x \right)$$

$$+ iJ_y \sum_{l=1}^{N/2-1} \left(\sigma_{4l-1}^y \sigma_{4l+1}^y - \sigma_{4l}^y \sigma_{4l+2}^y \right)$$

$$+ iB \sum_{l=1}^{N} (l-1)\left(\sigma_{2l-1}^z - \sigma_{2l}^z \right) + \gamma \sum_{l=1}^{N} \sigma_{2l-1}^z \sigma_{2l}^z - \gamma N. \quad (5)$$

In addition, the steady state transforms into $|\tilde{\rho}_s\rangle = \prod_{l=1}^{N}(|\uparrow_{2l-1}\uparrow_{2l}\rangle + |\downarrow_{2l-1}\downarrow_{2l}\rangle)/2$, for which only each two adjacent sites $2l - 1$ and $2l$ are entangled. Thus, it is a low-entangled state as mentioned earlier. Lastly, after this vectorization, the inner product of two operators $\text{tr}(\rho_1^\dagger \rho_2)$ can be expressed as $\langle\tilde{\rho}_1|\tilde{\rho}_2\rangle$.

With this methodology, we can now compute Eq. (3) on the transformed basis

$$C(t) = \langle\tilde{\mathbf{I}}|\sigma_{2N-1}^z e^{t\tilde{\mathcal{L}}}\sigma_{2N-1}^z|\tilde{\rho}_s\rangle, \tag{6}$$

which can be obtained by integrating its frequency components

$$C(t) = \int d^2\omega e^{\omega t}\mathcal{C}(\omega) \approx \sum_\omega (\Delta\omega)^2 e^{\omega t}\mathcal{C}(\omega) \tag{7}$$

with

$$\mathcal{C}(\omega) = \langle\tilde{\mathbf{I}}|\sigma_{2N-1}^z \delta^2(\omega - \tilde{\mathcal{L}})\sigma_{2N-1}^z|\tilde{\rho}_s\rangle, \tag{8}$$

where $\Delta\omega$ is the increment in ω when we discretize the integration into a summation. The Liouvilian is effectively a non-Hermitian operator, such that its dynamical correlator Eq. (8) can be computed with NHKPM [33], as detailed in Appendix B. Moreover, the short-range nature of $\tilde{\mathcal{L}}$ as well as the low entanglement in $\sigma_{2N-1}^z|\tilde{\rho}_s\rangle$ favors the implementation of NHKPM using the matrix-product state (MPS) representation.

III. RESULTS

We first consider $N = 4$, where the results are benchmarked with both exact diagonalization (ED) and the Runge-Kutta method in Appendix C. For concreteness, we consider $J_x = 0.75$, $J_y = 0.5$ throughout the whole manuscript. With a fixed dissipation rate, $\gamma = 0.2$, $\mathcal{C}(\omega)$ in Eq. (8) is computed for $B = 0, 0.13$, and 0.25 [Figs. 1(c)–1(e)], where we have presented the part of the spectrum featuring the peaks at the largest real frequency. We define $\Delta = |\max(\Re(\omega_i))|$ where ω_i are the center of the peaks of $\mathcal{C}(\omega)$, such that Δ characterizes the relaxation rate of $C(t)$ at long times: $C(t) \sim e^{-\Delta t}$. For $B = 0, 0.13$, and 0.25, we have $\Delta \approx 0.52, 0.53$, and 0.34, respectively. Using Eq. (7), we can now compute $C(t)$, as shown in Fig. 1(f) for short times, and in Fig. 1(g) for long times and in a log scale. We see that the time evolution agrees with the spectrum, namely, the long-time dynamics in all cases satisfy $C(t) \sim e^{-\Delta t}$.

To see how the long-time relaxation rate Δ changes with γ, we compute the projected correlator

$$\mathcal{C}_P(\Gamma) = \int d\Im\omega\mathcal{C}(\Gamma + i\Im\omega) \approx \sum_n \mathcal{C}(\Gamma + i\Im\omega_n)\Delta\omega, \tag{9}$$

which projects the dynamical correlator $\mathcal{C}(\omega)$ to the real axis. The smallest Γ at which $\mathcal{C}_P(\Gamma)$ exhibits a peak is thus equal to Δ by its definition. We note that the projected correlator is real as $\mathcal{C}(\Gamma + i\Im\omega) = \mathcal{C}^*(\Gamma - i\Im\omega)$, which is guaranteed by the universal property of Liouvillians $\mathcal{L}[\rho^\dagger] = (\mathcal{L}[\rho])^\dagger$. The change of $\mathcal{C}_P(\Gamma)$ as a function of γ for different B are shown in Fig. 2. We observe that for $B = 0$, Δ first increases linearly with γ, but then decreases after a critical point $\gamma_c \approx 0.6$. This is known as the quantum Zeno crossover [31,43].
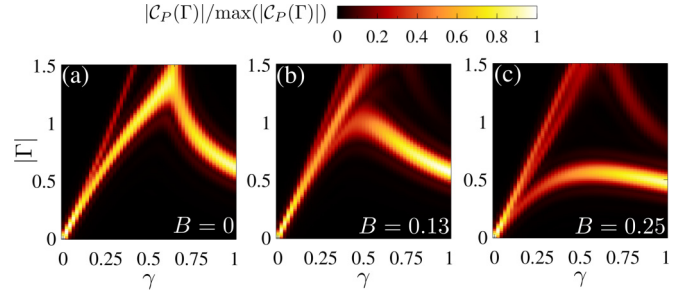

FIG. 2. The projected correlator of the Liouvillian $\mathcal{C}_P(\Gamma)$ in Eq. (9), computed with $N = 4$ and varying γ for $B = 0, 0.13$, and 0.25 in panels (a)–(c), respectively; showing how the long-time relaxation rate Δ changes with γ and B. Compared to $B = 0$, Δ is decreased for $B = 0.25$ when γ is small due to Stark localization. However, this effect is hindered by the finite-size effect for $B = 0.13$.

This crossover implies that the Liouvillian dynamics with a weak γ and with a strong γ are dominated by different physical factors. The properties of the Hamiltonian are crucial in the weak γ regime, whereas the dissipative effects induced by dissipators take the main charge in the strong γ regime. Consequently, the gradient magnetic field B which can cause Stark localization in the Hamiltonian is expected to significantly influence the relaxation rate Δ within the weak γ regime.

Increasing the magnetic field gradient B is known to result in stronger localization of the eigenstates $\{|n\rangle\}$ of H [39,40]. In particular, when $B \gg J_{x,y}$, $|n\rangle$ will become localized enough to be also the eigenstates of all dissipators $L_l = \sigma_l^z$. In such a case, $\{|n\rangle\langle n|\}$ will span a decoherence-free space with zero relaxation rate. For a smaller B, the relaxation rate of this space is lifted due to the finite localization length of $|n\rangle$. As a result, the stronger the localization is, the smaller the relaxation rate becomes. This shows that Stark localization in the Hamiltonian can slow down the dynamics of the Liouvillian. A similar phenomenon was observed in a fermionic model [49]. In our model, the reduction of the relaxation rate Δ in the weak γ regime is observed for $B = 0.25$ from both the autocorrelator $C(t)$ in Fig. 1(g) and the projected correlator $\mathcal{C}_P(\Gamma)$ in Fig. 2. However, for $B = 0.13$, due to the finite-size effect, the localization length of the states is still larger than the system size $N = 4$, and the reduction of the relaxation rate stemming from the localization is not seen.

To overcome finite-size effects, we now move on to consider a larger system size $N = 20$. It is important that for our model, increasing the system size would not significantly shorten the weak γ regime we are interested in. This is different from the previously studied models with $U(1)$ symmetry [49–51], for which the weak γ regime shrinks to zero in the thermodynamic limit [10]. It is worth noting that, although our model with a finite B is not solvable, its special structure still decouples the evolution of two-point correlators from other higher-order correlators. This property allows us to benchmark our results obtained from NHKPM by diagonalizing a "damping matrix" of dimension $4N^2$ in Appendix D.

We compute the autocorrelator $C(t)$ via combining the results of $\mathcal{C}(\omega)$ obtained from NHKPM with Eq. (7). To reduce the computational cost, we first compute $\mathcal{C}(\omega)$ in a large area in the complex plane to identify
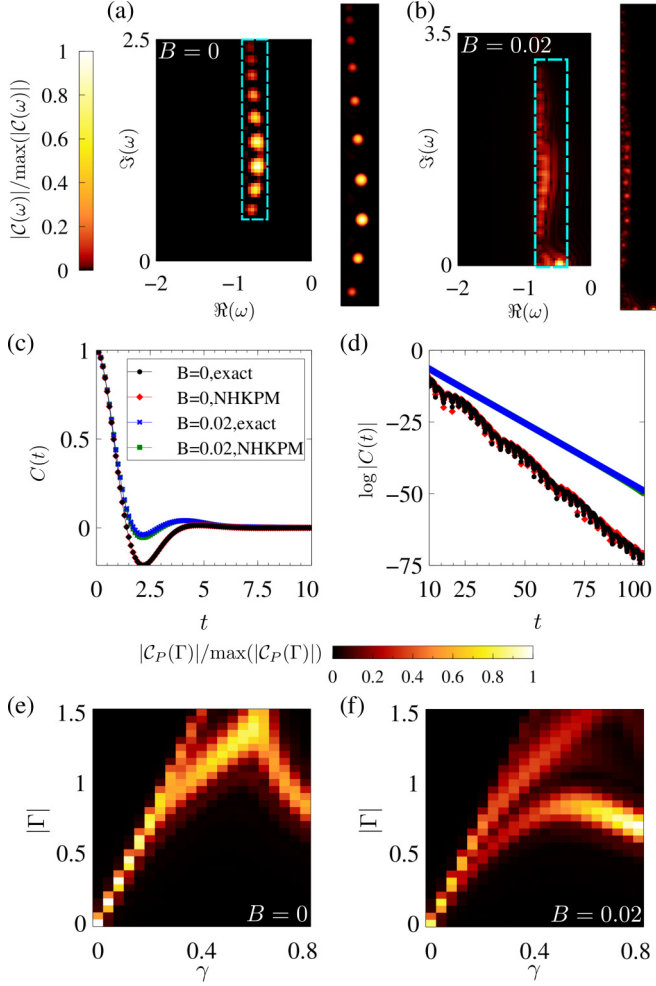
FIG. 3. The Liouvillian dynamics for $N = 20$. (a), (b) The dynamical correlator $\mathcal{C}(\omega)$ in Eq. (8) computed with $\gamma = 0.2$ for $B = 0$ and $B = 0.02$, respectively. The insets show the $\mathcal{C}(\omega)$ computed with a higher resolution in the region specified with cyan rectangles. (c), (d) The autocorrelator $C(t)$ in Eq. (6) for $B = 0$ and $B = 0.02$ computed exactly by diagonalizing the "damping matrix" and with NHKPM. Panel (d) has the same labels as panel (c). Compared to $B = 0$, the long-time relaxation rate Δ is decreased for $B = 0.02$. (e), (f) The projected correlator of the Liouvillian $\mathcal{C}_P(\Gamma)$ computed with varying γ for $B = 0$ and $B = 0.02$, respectively. Compared to $B = 0$, Δ is decreased for $B = 0.02$ for small γ, showing that the finite-size effect has been eliminated compared to Fig. 2(b).

the region where it shows peaks, and then compute it with a better frequency resolution in this specific region [insets in Figs. 3(a) and 3(b)]. We see that NHKPM allows to faithfully extract $C(t)$, as the results agree with the exact results obtained by diagonalizing the "damping matrix" [Figs. 3(c) and 3(d)]. From Fig. 3(d), it is obvious that even a rather small B can lead to a slower long-time decay of $C(t)$ compared to $B = 0$. To further demonstrate the decrease of Δ with increasing B in the whole weak γ regime, we show the projected correlator $\mathcal{C}_P(\Gamma)$ in Eq. (9) with varying γ for both $B = 0$ and $B = 0.02$ [Figs. 3(e) and 3(f)]. In contrast to the case of $N = 4$ and $B = 0.13$, in the case of $N = 20$ and $B = 0.02$, the decrease of Δ compared to $B = 0$ is observed, showing that in this case finite-size effects are eliminated.
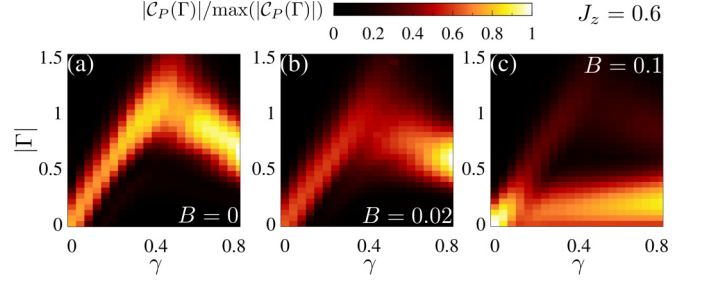

FIG. 4. The projected correlator of the Liouvillian $\mathcal{C}_P(\Gamma)$ in Eq. (9), computed with $N = 20$ and $J_z = 0.6$; $B = 0$ in (a), $B = 0.02$ in (b), and $B = 0.1$ in (c). (a) The presence of a finite J_z reduces the quantum Zeno crossover point to around $\gamma_c \approx 0.4$. (b) The reduction of Δ in the presence of $B = 0.02$ is less significant compared to Fig. 3(f) due to a finite threshold in B to cause Stark localization. (c) For a larger $B = 0.1$, the reduction of Δ becomes visible.

Finally, we include an interaction term to the Hamiltonian of the form $\sum_{l=1}^{N-1} J_z \sigma_l^z \sigma_{l+1}^z$. With this interaction term, it is no longer possible to solve the spectrum and dynamics with exact methods, while NHKPM can still be applied. We are particularly interested in how this interaction influences the quantum Zeno crossover and the reduction of the relaxation rate due to Stark localization. For concreteness, we take $J_z = 0.6$ in our analysis. We observe that when $B = 0$, the quantum Zeno crossover point γ_c is reduced compared to the case $J_z = 0$ [Fig. 4(a)]. This reduction of γ_c can be understood from the fact that when $J_z \to \infty$, the model will have $U(1)$ symmetry, resulting in $\gamma_c = 0$ in the thermodynamic limit [49–51]; a finite J_z does not fully restore this symmetry, but can still reduce γ_c. Stark localization in noninteracting systems takes place with an infinitesimal gradient potential. In contrast, the introduction of the interaction $\sum_{l=1}^{N-1} J_z \sigma_l^z \sigma_{l+1}^z$ leads to Stark many-body localization only when the gradient B is above a finite threshold [42]. This is consistent with our numerical findings, as the reduction of the relaxation with a small $B = 0.02$ is not significant, as shown in Fig. 4(b). However, such relaxation becomes visible for a larger $B = 0.1$ [Fig. 4(c)].

IV. CONCLUSION

We have demonstrated a method to solve many-body Liouvillian dynamics based on NHKPM and tensor-network techniques. This method allows to compute the dynamical correlator of a many-body Liouvillian, providing access to the Liouvillian spectrum and Liouvillian dynamics. Focusing on the dephasing quantum compass model with a gradient magnetic field, we have demonstrated the faithfulness of our method by comparing it with exact results. This enabled the characterization of the quantum Zeno crossover and the reduction of relaxation rate due to Stark localization in our model. We further demonstrated the capabilities of our method in regimes where previous exact methods cannot be applied, in particular by exploring how nearest-neighbor interactions influence the Liouvillian dynamics of our model. Compared to existing tensor-network methods for open quantum dynamics such as TEBD [38,52,53] and TDVP [54,55], our method focuses on the computation of the dynamical correlator $\mathcal{C}(\omega)$ instead of the autocorrelator $C(t)$. The autocorrelator $C(t)$ can

be determined by the dynamical correlator $\mathcal{C}(\omega)$, while the converse is not true. In this sense, our method can provide more information to explore the underlying mechanisms of the open quantum dynamics. Specifically, the long-time relaxation rate can be directly extracted from $\mathcal{C}(\omega)$. Additionally, our method is particularly favorable for computing long-time dynamics as the computational cost of $C(t)$ from $\mathcal{C}(\omega)$ does not increase with t. Our method can be applied to a variety of open quantum many-body systems with short-range interactions [53,56–59]. The dynamical correlators computed with our method would allow to explore interesting properties such as the Liouvillian gap and novel non-Hermitian topology of these systems. Finally, beyond its fundamental interest, our methodology would allow rationalizing dynamical correlators at complex frequencies measured experimentally [60,61].

APPENDIX A: VECTORIZATION OF A DENSITY MATRIX

In this section, we explain the choice of basis for the vectorization of a density matrix. The most intuitive way of vectorizing ρ for our model $\mathcal{L}$ is

$$\rho = \sum_{\sigma_1 \cdots \sigma_N} \sum_{\tau_1 \cdots \tau_N} \rho_{\sigma_1 \cdots \sigma_N \tau_1 \cdots \tau_N} |\sigma_1 \cdots \sigma_N\rangle\langle\tau_1 \cdots \tau_N|$$

$$\rightarrow |\tilde{\rho}\rangle = \sum_{\sigma_1 \cdots \sigma_N} \sum_{\tau_1 \cdots \tau_N} \rho_{\sigma_1 \cdots \sigma_N \tau_1 \cdots \tau_N} |\sigma_1 \cdots \sigma_N\rangle|\tau_1 \cdots \tau_N\rangle. \quad \text{(A1)}$$

Under this basis choice, the transformed Liouvillian is

$$\tilde{\mathcal{L}} = -iH \otimes \mathbf{I} + i\mathbf{I} \otimes H^T$$
$$+ \sum_l \left(L_l \otimes L_l^* - \frac{1}{2}\left(L_l^\dagger L_l \otimes \mathbf{I} + \mathbf{I} \otimes L_l^T L_l^*\right)\right)$$
$$= iJ_x \sum_{l=1}^{N/2} \left(\sigma_{2l-1}^x \sigma_{2l}^x - \sigma_{2l-1+N}^x \sigma_{2l+N}^x\right)$$
$$+ iJ_y \sum_{l=1}^{N/2-1} \left(\sigma_{2l}^y \sigma_{2l+1}^y - \sigma_{2l+N}^y \sigma_{2l+1+N}^y\right)$$
$$+ iB \sum_{l=1}^{N}(l-1)\left(\sigma_l^z - \sigma_{l+N}^z\right) + \gamma \sum_{l=1}^{N} \sigma_l^z \sigma_{l+N}^z - \gamma N, \quad \text{(A2)}$$

where H and L_l are given in Eq. (1) in the main text. We see that in Eq. (A2) long-range interactions $\sigma_l^z \sigma_{l+N}^z$ exist, in

particular when N is large. This is not favorable for calculations with tensor networks. In addition, under this basis, the steady state $\rho_s = \mathbf{I}/2^N$ transforms into:

$$|\tilde{\rho}_s\rangle = \frac{1}{2^N} \sum_{\sigma_1 \cdots \sigma_{2N}} \delta_{\sigma_1 \sigma_{N+1}} \delta_{\sigma_2 \sigma_{N+2}} \cdots \delta_{\sigma_N \sigma_{2N}} |\sigma_1 \cdots \sigma_{2N}\rangle, \quad \text{(A3)}$$

which lacks a simple matrix-product-state (MPS) representation. For both reasons, we choose the basis in Eq. (4) for vectorization where spin indices have been permuted.

APPENDIX B: DYNAMICAL CORRELATORS WITH NHKPM

From our previous work [33], we derived that an arbitrary dynamical correlator

$$f(\omega) = \langle\psi_{\mathrm{L}}|\delta^2(\omega - \tilde{\mathcal{L}})|\psi_{\mathrm{R}}\rangle \quad \text{(B1)}$$

is equal to

$$f(\omega) = \partial_{\omega^*}\langle\psi_{\mathrm{L}}|(\omega - \tilde{\mathcal{L}})^{-1}|\psi_{\mathrm{R}}\rangle$$
$$= \sum_n \partial_{\omega^*}(\omega - \omega_n)^{-1}\langle\psi_{\mathrm{L}}|\psi_{\mathrm{R,n}}\rangle\langle\psi_{\mathrm{L,n}}|\psi_{\mathrm{R}}\rangle, \quad \text{(B2)}$$

where ω_n and $|\psi_{\mathrm{R(L),n}}\rangle$ are the nth eigenvalue and right (left) eigenvector of $\tilde{\mathcal{L}}$. Thus, Eq. (B1) can be computed with

$$f(\omega) = \frac{1}{\pi}\partial_{\omega^*}G(E=0), \quad \text{(B3)}$$

where

$$G(E) = \langle\mathrm{L}|(E - \mathcal{H})^{-1}|\mathrm{R}\rangle \quad \text{(B4)}$$

is an entry of the Green's function of the Hermitrized Hamiltonian $\mathcal{H}$:

$$\mathcal{H} = \begin{pmatrix} & \omega - \tilde{\mathcal{L}} \\ \omega^* - \tilde{\mathcal{L}}^\dagger & \end{pmatrix} \quad \text{(B5)}$$

with

$$|\mathrm{L}\rangle = \begin{pmatrix} 0 \\ |\psi_{\mathrm{L}}\rangle \end{pmatrix}, \quad |\mathrm{R}\rangle = \begin{pmatrix} |\psi_{\mathrm{R}}\rangle \\ 0 \end{pmatrix}. \quad \text{(B6)}$$

Since $G(E)$ is a function of a single variable, we can apply the kernel polynomial method (KPM) to compute $G(E)$, giving

$$G_{\mathrm{KPM}}(E=0) = \sum_n \langle\mathrm{L}|\varphi_n\rangle\left(\mathcal{E}_n^{-1}\right)_{\mathrm{KPM}}\langle\varphi_n|\mathrm{R}\rangle, \quad \text{(B7)}$$

where $\mathcal{E}_n$ and $|\varphi_n\rangle$ are the nth eigenvalue and eigenvector of $\mathcal{H}$. The approximated function $(\mathcal{E}_n^{-1})_{\mathrm{KPM}}$ depends on the kernel function and the number of polynomials in the Chebyshev expansion [35]. In particular, for calculations in the main text, we have chosen the Jackson kernel, resulting in

$$\left(\frac{1}{\mathcal{E}_n}\right)_{\mathrm{J}} \approx \frac{2}{\sqrt{2\sigma^2}}F\left(\frac{\mathcal{E}_n}{\sqrt{2\sigma^2}}\right), \quad \text{(B8)}$$

where $F(x) = \exp(-x^2)\int_0^x \exp(t^2)dt$ is the Dawson function [63] and $\sigma = \pi/N$ where N is the number of polynomials in the Chebyshev expansion. Equation (B8) provides a good approximation for $1/\mathcal{E}_n$ for $\mathcal{E}_n \gtrsim 2\sigma$:

$$\frac{2}{\sqrt{2\sigma^2}}F\left(\frac{\mathcal{E}_n}{\sqrt{2\sigma^2}}\right) = \frac{1}{\mathcal{E}_n} + O\left(\frac{\sigma^2}{\mathcal{E}_n^3}\right) \quad (\mathcal{E}_n \gtrsim 2\sigma). \quad \text{(B9)}$$

From Eq. (B5) we see that $\mathcal{E}_n = \pm|\omega - \omega_n|$, where ω_n are the eigenvalues of $\tilde{\mathcal{L}}$. Thus, the KPM approximates $|\omega - \omega_n|^{-1}$ with $(|\omega - \omega_n|^{-1})_J$:

$$f_{\text{KPM}}(\omega)$$

$$= \sum_n \partial_{\omega^*} \left[\left(\frac{1}{|\omega - \omega_n|} \right)_J e^{-i \arg(\omega - \omega_n)} \right] \langle \psi_L | \psi_{R,n} \rangle \langle \psi_{L,n} | \psi_R \rangle$$

$$= \sum_n \partial_{\omega^*} \left[\left(\frac{1}{|\omega - \omega_n|} \right)_J \frac{|\omega - \omega_n|}{\omega - \omega_n} \right] \langle \psi_L | \psi_{R,n} \rangle \langle \psi_{L,n} | \psi_R \rangle.$$

(B10)

We now demonstrate that $f_{\text{KPM}}(\omega)$ provides a good approximation to $f(\omega)$ upon integration. Let

$$g(\omega - \omega_n) = \left(\frac{1}{|\omega - \omega_n|} \right)_J \frac{|\omega - \omega_n|}{\omega - \omega_n},$$

(B11)

and note that for a region Σ in the complex plane,

$$\int_\Sigma d^2\omega \partial_{\omega^*} g(\omega - \omega_n)$$

$$= \frac{1}{2} \int_\Sigma d^2\omega (\partial_x g(\omega - \omega_n) - \partial_y (ig(\omega - \omega_n)))$$

$$= \frac{1}{2} \int_{d\Sigma} (g(\omega - \omega_n), ig(\omega - \omega_n)) \cdot d\mathbf{l},$$

(B12)

where we have used the Stokes theorem. From Eq. (B9) we see that as long as $|\omega - \omega_n| > 2\sigma$, when $\omega \in d\Sigma$, $g(\omega - \omega_n) \approx (\omega - \omega_n)^{-1}(1 + O(\sigma^2|\omega - \omega_n|^{-2}))$ will also hold for $\omega \in d\Sigma$, and Eq. (B12) reduces to

$$\int_\Sigma d^2\omega \partial_{\omega^*} g(\omega - \omega_n)$$

$$\approx \frac{1}{2} \int_{d\Sigma} ((\omega - \omega_n)^{-1}, i(\omega - \omega_n)^{-1}) \cdot d\mathbf{l}$$

$$= \int_\Sigma d^2\omega \partial_{\omega^*} (\omega - \omega_n)^{-1}.$$

(B13)

Thus, when a complex plane Σ satisfy $|\omega - \omega_n| > 2\sigma, \forall \omega \in d\Sigma, \forall n$, we will have

$$\int_\Sigma d^2\omega f_{\text{KPM}}(\omega) \approx \int_\Sigma d^2\omega f(\omega).$$

(B14)

The error decreases as Σ becomes larger, and in particular, if Σ is the whole complex plane then both sides of Eq. (B14) are equal. Note that when σ is small enough, which can be achieved with a larger number of polynomials N, Eq. (B14) will hold in a small region containing only one specific eigenvalue ω_i. This means that the spectral weight of this eigenvalue computed with NHKPM is equal to its exact value.

We have thus shown that, NHKPM not only allows to predict the eigenvalues of $\tilde{\mathcal{L}}$, as demonstrated in our previous work [33], but it also correctly predicts the spectral weight of the eigenvalues. This essentially enables the calculation of the autocorrelator from dynamical correlators with Eq. (7) in the main text.

We now move on to show that NHKPM maintains an important property of the dynamical correlator $\mathcal{C}(\omega)$ that ensures the autocorrelator $C(t)$ to be real. The autocorrelator is

computed as

$$C(t) = \int d^2\omega e^{\omega t} \mathcal{C}(\omega),$$

(B15)

where

$$\mathcal{C}(\omega) = \langle \tilde{\mathbf{I}} | \sigma_{2N-1}^z \delta^2(\omega - \tilde{\mathcal{L}}) \sigma_{2N-1}^z | \tilde{I} \rangle / 2^N.$$

(B16)

We note that the eigen-operators of $\mathcal{L}$ are either Hermitian or in pairs of Hermitian conjugation [23]:

$$\mathcal{L}[\rho_n^\dagger] = \omega_n^* \rho_n^\dagger \text{ if } \mathcal{L}[\rho_n] = \omega_n \rho_n,$$

(B17)

or in the transformed form

$$\tilde{\mathcal{L}} |\widetilde{\rho_n^\dagger}\rangle = \omega_n^* |\widetilde{\rho_n^\dagger}\rangle \text{ if } \tilde{\mathcal{L}} |\tilde{\rho}_n\rangle = \omega_n |\tilde{\rho}_n\rangle.$$

(B18)

As a consequence, if ρ is Hermitian, we have

$$\langle \tilde{\rho} | \delta^2(\omega - \tilde{\mathcal{L}}) | \tilde{\rho} \rangle = \sum_n \delta^2(\omega - \omega_n^*) \langle \tilde{\rho} | \widetilde{\rho_n^\dagger} \rangle \langle \widetilde{\rho_{L,n}^\dagger} | \tilde{\rho} \rangle$$

$$= \sum_n \delta^2(\omega - \omega_n^*) \langle \widetilde{\rho^\dagger} | \widetilde{\rho_n^\dagger} \rangle \langle \widetilde{\rho_{L,n}^\dagger} | \widetilde{\rho^\dagger} \rangle$$

$$= \left(\sum_n \delta^2(\omega - \omega_n^*) \langle \tilde{\rho} | \tilde{\rho}_n \rangle \langle \tilde{\rho}_{L,n} | \tilde{\rho} \rangle \right)^*$$

$$= \left(\langle \tilde{\rho} | \delta^2(\omega - \tilde{\mathcal{L}}) | \tilde{\rho} \rangle \right)^*,$$

(B19)

where $\langle \tilde{\rho}_{L,n} |$ is the left eigenvector of $\tilde{\mathcal{L}}$ corresponding to eigenvalue ω_n. We have used Eq. (B18) in deriving the second line of Eq. (B19). Since $\rho = \sigma_N^z \mathbf{I}$ is Hermitian, we have

$$\mathcal{C}(\omega^*) = \mathcal{C}^*(\omega),$$

(B20)

an important property that ensures $C(t)$ is real. We see that the results obtained with NHKPM maintain this property (Fig. 5).

APPENDIX C: DYNAMICS WITH ED AND RUNGE-KUTTA METHOD FOR $N = 4$

We present the numerical details for computing the autocorrelator $C(t)$ with exact diagonalization (ED) and the Runge-Kutta methods. We note that

$$C(t) = \text{tr}(\sigma_N^z(t) \sigma_N^z(0) \rho_s) = \text{tr}(\sigma_N^z e^{t\mathcal{L}} [\sigma_N^z \rho_s])$$

(C1)

when the Liouvillian is treated as a superoperator, and

$$C(t) = \langle \tilde{\mathbf{I}} | \sigma_{2N-1}^z e^{t\tilde{\mathcal{L}}} \sigma_{2N-1}^z | \tilde{\rho}_s \rangle$$

(C2)

in the vectorized form.

To compute $C(t)$ with ED, we use Eq. (C2), and diagonalize $\tilde{\mathcal{L}}$:

$$\tilde{\mathcal{L}} = \sum_n \omega_n |\tilde{\rho}_n\rangle \langle \tilde{\rho}_{n,L}|$$

(C3)

such that $C(t)$ can be computed with

$$C(t) = \sum_n \langle \tilde{\mathbf{I}} | \sigma_{2N-1}^z | \tilde{\rho}_n \rangle e^{\omega_n t} \langle \tilde{\rho}_{n,L} | \sigma_{2N-1}^z | \tilde{\rho}_s \rangle.$$

(C4)

To compute $C(t)$ with the Runge-Kutta method, we can directly use Eq. (C1) without the need for vectorization. Let
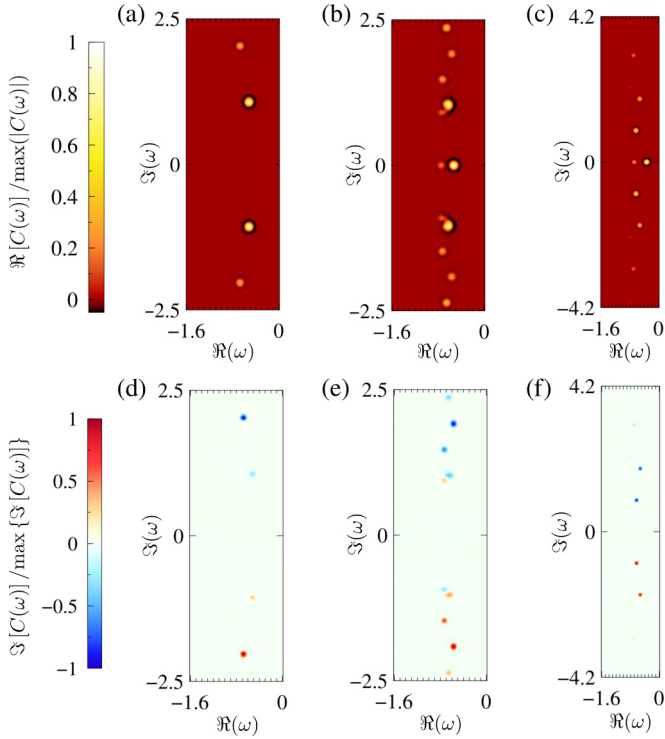
$$y(t) = e^{t\mathcal{L}} [\sigma_N^z \rho_s];$$

(C5)

FIG. 5. Real and imaginary parts of the dynamical correlator $\mathcal{C}(\omega)$ in Figs. 1(c)–1(e) in the main text. Panels (a) and (d) are computed with $B = 0$, panels (b) and (e) are computed with $B = 0.13$, and panels (c) and (f) are computed with $B = 0.25$. We see that the computed $\mathcal{C}(\omega)$ satisfy $\mathcal{C}(\omega^*) = \mathcal{C}^*(\omega)$.

we have

$$\frac{dy}{dt} = \mathcal{L}[y(t)] \equiv f(y) \tag{C6}$$

with $y(t = 0) = \sigma_N^z \rho_s$. This allows us to use the Runge-Kutta method [64] to iteratively compute $y(t)$ with a time step of h:

$$y_{n+1} = y_n + \frac{h}{6}(k_1 + 2k_2 + 2k_3 + k_4)$$

$$t_{n+1} = t_n + h, \tag{C7}$$

where

$$k_1 = f(y_n)$$

$$k_2 = f\left(y_n + h\frac{k_1}{2}\right)$$

$$k_3 = f\left(y_n + h\frac{k_2}{2}\right)$$

$$k_4 = f(y_n + hk_3) \tag{C8}$$

with $y_0 = \sigma_N^z \rho_s$ and $t_0 = 0$.

The computations of $C(t)$ in Figs. 1(f) and 1(g) in the main text with both ED and Runge-Kutta method are shown in Fig. 6, where both results verify the correctness of NHKPM in computing $C(t)$.
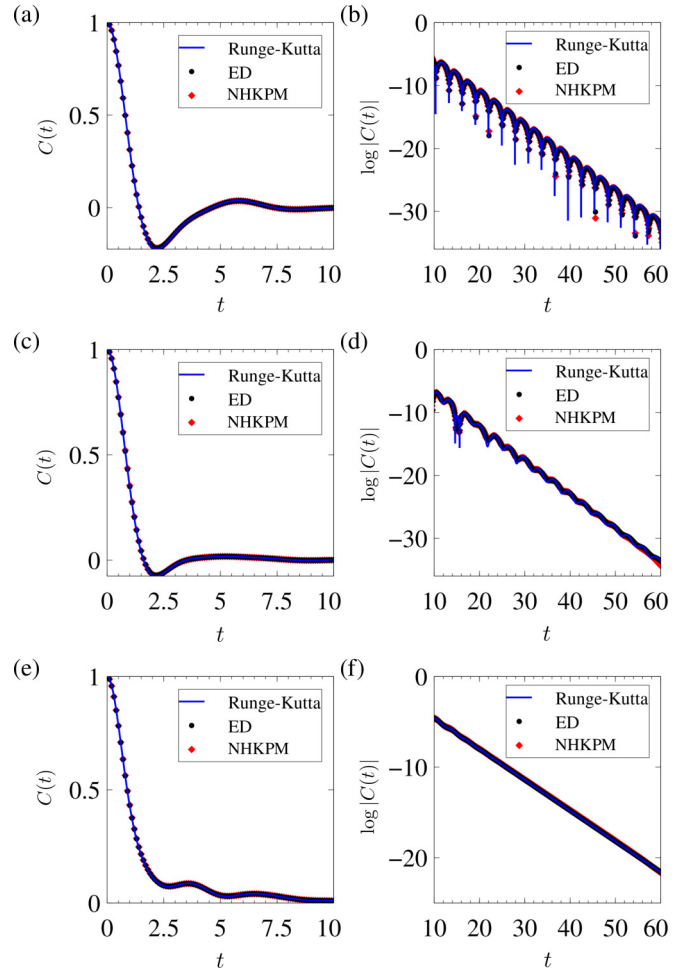

FIG. 6. Benchmark of $C(t)$ in Figs. 1(f) and 1(g) in the main text. Panels (a) and (b) are computed with $B = 0$, panels (c) and (d) are computed with $B = 0.13$, and panels (e) and (f) are computed with $B = 0.25$. The results with both ED and Runge-Kutta methods agree with the results obtained with NHKPM.

APPENDIX D: DYNAMICS OBTAINED USING THE CLOSED HIERARCHY OF CORRELATIONS FOR $N = 20$

To compute $C(t)$ in the case of $N = 20$, both ED and the Runge-Kutta method fail due to the exponentially large Hilbert space. However, in our model, the Liouvillian preserves two-point correlators, allowing us to compute the dynamics by diagonalizing a "damping matrix" [44,45]. We present the numerical details below.

It is simpler to deal with the quantum compass model under the Majorana basis [29]. This is done by performing the Jordan-Wigner transformation [65]

$$\sigma_l^+ = \prod_{j<l} e^{i\pi n_j} c_l^\dagger$$

$$\sigma_l^- = c_l \prod_{j<l} e^{-i\pi n_j}$$

$$\sigma_l^z = 2c_l^\dagger c_l - 1 \tag{D1}$$

to transform the spin model into a fermion model, followed by a transformation into the following Majorana

basis:

$$\gamma_l^- = i(c_i - c_i^\dagger), \quad \gamma_l^+ = (c_i + c_i^\dagger) \quad (l \quad \text{odd}),$$
$$\gamma_l^- = (c_i + c_i^\dagger), \quad \gamma_l^+ = i(c_i - c_i^\dagger) \quad (l \quad \text{even}), \quad \text{(D2)}$$

where it can be verified $\{\gamma_l^\alpha, \gamma_j^\beta\} = 2\delta_{\alpha\beta}\delta_{lj}$. An important property of the Majorana operators is

$$[\gamma_i\gamma_j, \gamma_l\gamma_m] = 2\gamma_i\gamma_m\delta_{jl} - 2\gamma_i\gamma_l\delta_{jm} + 2\gamma_m\gamma_j\delta_{il} - 2\gamma_l\gamma_j\delta_{im}, \quad \text{(D3)}$$

which ensures the commutator of two quadratic operators is still quadratic. A Hermitian quadratic operator A under the Majorana basis is:

$$A = \frac{i}{4}\vec{\gamma}^T a \vec{\gamma} \quad \text{(D4)}$$

with $a = -a^T$, where

$$\vec{\gamma} = \begin{pmatrix} \gamma_1^- \\ \vdots \\ \gamma_N^- \\ \gamma_1^+ \\ \vdots \\ \gamma_N^+ \end{pmatrix}. \quad \text{(D5)}$$

In particular, in our model, both the Hamiltonian H and the Lindblad dissipators are Hermitian, which ensures the preservation of two-point correlators. Furthermore, the density matrix $O = \sigma_N^z \rho_{ss}$ is also Hermitian. Thus, the time evolution can be computed in the single-particle subspace of Majorana fermions. In the Majorana basis, the Hamiltonian H can be expressed as

$$H = \frac{i}{4}\vec{\gamma}^T h \vec{\gamma}, \quad \text{(D6)}$$

where

$$h = \begin{pmatrix} T & M \\ -M & \end{pmatrix} \quad \text{(D7)}$$

with

$$T = \begin{pmatrix} 0 & 2J_x & 0 & 0 \\ -2J_x & 0 & -2J_y & 0 \\ 0 & 2J_y & 0 & 2J_x \\ 0 & 0 & \ddots & \ddots \end{pmatrix} \quad \text{(D8)}$$

and

$$M = \begin{pmatrix} 0 & & & \\ & 2B & & \\ & & 4B & \\ & & & \ddots \end{pmatrix}. \quad \text{(D9)}$$

Similarly, the Lindblad dissipator $L_l = \sqrt{\gamma}\sigma_l^z$ becomes

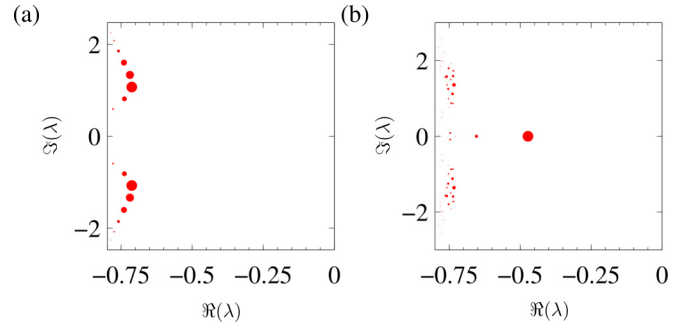$$L_l = \frac{i}{4}\vec{\gamma}^T l_l \vec{\gamma}, \quad \text{(D10)}$$

FIG. 7. Spectrum of the damping matrix X in Eq. (D16) with $N = 20$ and $B = 0$ in panel (a), and $B = 0.02$ in panel (b). The spectrum is highlighted with red color, and the size of the dots is proportional to $\langle nL|\tilde{o}(0)\rangle$, the overlap between the corresponding eigenstate of the eigenvalue and the state $|\tilde{o}(0)\rangle$.

where

$$l_l = \begin{pmatrix} 0 & \tilde{l}_l \\ -\tilde{l}_l & 0 \end{pmatrix} \quad \text{(D11)}$$

with

$$(\tilde{l}_l)_{ij} = 2\sqrt{\gamma}\delta_{il}\delta_{jl}. \quad \text{(D12)}$$

Finally, the density matrix O can also be expanded

$$O = \frac{i}{4}\vec{\gamma}^T o \vec{\gamma}. \quad \text{(D13)}$$

When the dissipators L_l are Hermitian, the quantum master equation becomes

$$\frac{d}{dt}O = -i[H, O] - \frac{1}{2}\sum [L_l, [L_l, O]]. \quad \text{(D14)}$$

Under the Majorana basis, this is

$$\frac{d}{dt}o = [h, o] - \frac{1}{2}\sum [l_l, [l_l, o]]$$
$$= ho - oh - \sum_l l_l o l_l - 4\gamma o. \quad \text{(D15)}$$

In the vectorized form, Eq. (D15) becomes

$$\frac{d}{dt}|\tilde{o}\rangle = \left[\left(h \otimes \mathbf{1} - \mathbf{1} \otimes h^T - \sum_l l_l \otimes l_l^T\right) - 4\gamma \mathbf{1} \otimes \mathbf{1}\right]|\tilde{o}\rangle,$$
$$= X|\tilde{o}\rangle. \quad \text{(D16)}$$

where the $4N^2 \times 4N^2$ matrix X is called the damping matrix, with N being the length of the spin chain. Diagonalizing the damping matrix as

$$X = \sum_n \lambda_n |nR\rangle \langle nL|, \quad \text{(D17)}$$

we have

$$|\tilde{o}(t)\rangle = \sum_n e^{\lambda_n t} |nR\rangle \langle nL|\tilde{o}(0)\rangle, \quad \text{(D18)}$$

and this allows to compute $C(t) = \mathrm{tr}(\sigma_N^z O(t))$ as

$$C(t) = \langle \tilde{s}_N^z | \tilde{o}(t) \rangle, \tag{D19}$$

where $|\tilde{s}_N^z\rangle$ is the vectorized form of s_N^z, and s_N^z is the representation of σ_N^z under the Majorana basis:

$$\sigma_N^z = \frac{i}{4} \vec{\gamma}^T s_N^z \vec{\gamma}. \tag{D20}$$

In Fig. 7, it is shown the spectrum of the damping matrix X for $N = 20$ and $B = 0$ and $B = 0.02$, respectively. In the nonsolvable case $B = 0.02$, the spectrum is more complicated than the solvable case $B = 0$. The spectrum also indicates a long-time relaxation rate of $\Delta = 0.65$ for $B = 0$, and $\Delta = 0.47$ for $B = 0.02$, in agreement with the results in Fig. 3 in the main text.

[1] A. Polkovnikov, K. Sengupta, A. Silva, and M. Vengalattore, Colloquium: Nonequilibrium dynamics of closed interacting quantum systems, Rev. Mod. Phys. **83**, 863 (2011).

[2] L. M. Sieberer, M. Buchhold, J. Marino, and S. Diehl, Universality in driven open quantum matter, arXiv:2312.03073.

[3] F. Verstraete, M. M. Wolf, and J. Ignacio Cirac, Quantum computation and quantum-state engineering driven by dissipation, Nat. Phys. **5**, 633 (2009).

[4] S. Diehl, W. Yi, A. J. Daley, and P. Zoller, Dissipation-induced d-wave pairing of fermionic atoms in an optical lattice, Phys. Rev. Lett. **105**, 227001 (2010).

[5] C.-E. Bardyn, M. A. Baranov, E. Rico, A. İmamoğlu, P. Zoller, and S. Diehl, Majorana modes in driven-dissipative atomic superfluids with a zero chern number, Phys. Rev. Lett. **109**, 130402 (2012).

[6] M. Nakagawa, N. Tsuji, N. Kawakami, and M. Ueda, η pairing of light-emitting fermions: Nonequilibrium pairing mechanism at high temperatures, arXiv:2103.13624.

[7] X. Mi *et al.*, Stable quantum-correlated many-body states through engineered dissipation, Science **383**, 1332 (2024).

[8] Z. Cai and T. Barthel, Algebraic versus exponential decoherence in dissipative many-particle systems, Phys. Rev. Lett. **111**, 150403 (2013).

[9] B. Olmos, I. Lesanovsky, and J. P. Garrahan, Facilitated spin models of dissipative quantum glasses, Phys. Rev. Lett. **109**, 020403 (2012).

[10] M. Žnidarič, Relaxation times of dissipative many-body quantum systems, Phys. Rev. E **92**, 042143 (2015).

[11] R. Bouganne, M. Bosch Aguilera, A. Ghermaoui, J. Beugnon, and F. Gerbier, Anomalous decay of coherence in a dissipative many-body system, Nat. Phys. **16**, 21 (2020).

[12] J. Ren, Q. Li, W. Li, Z. Cai, and X. Wang, Noise-driven universal dynamics towards an infinite temperature state, Phys. Rev. Lett. **124**, 130602 (2020).

[13] H.-R. Wang, D. Yuan, S.-Y. Zhang, Z. Wang, D.-L. Deng, and L.-M. Duan, Embedding quantum many-body scars into decoherence-free subspaces, Phys. Rev. Lett. **132**, 150401 (2024).

[14] K. Wang, F. Piazza, and D. J. Luitz, Hierarchy of relaxation timescales in local random liouvillians, Phys. Rev. Lett. **124**, 100604 (2020).

[15] J. L. Li, D. C. Rose, J. P. Garrahan, and D. J. Luitz, Random matrix theory for quantum and classical metastability in local liouvillians, Phys. Rev. B **105**, L180201 (2022).

[16] F. Song, S. Yao, and Z. Wang, Non-hermitian skin effect and chiral damping in open quantum systems, Phys. Rev. Lett. **123**, 170401 (2019).

[17] T. Haga, M. Nakagawa, R. Hamazaki, and M. Ueda, Liouvillian skin effect: Slowing down of relaxation processes without gap closing, Phys. Rev. Lett. **127**, 070402 (2021).

[18] N. Okuma and M. Sato, Quantum anomaly, non-hermitian skin effects, and entanglement entropy in open systems, Phys. Rev. B **103**, 085428 (2021).

[19] W. Chen, M. Abbasi, B. Ha, S. Erdamar, Y. N. Joglekar, and K. W. Murch, Decoherence-induced exceptional points in a dissipative superconducting qubit, Phys. Rev. Lett. **128**, 110402 (2022).

[20] P.-X. Shen, Z. Lu, J. L. Lado, and M. Trif, Non-hermitian persistent current transport, Phys. Rev. Lett. **133**, 086301 (2024).

[21] R. D. Soares and M. Schirò, Non-unitary quantum many-body dynamics using the faber polynomial method, SciPost Phys. **17**, 128 (2024).

[22] H. Breuer and F. Petruccione, *The Theory of Open Quantum Systems* (Oxford University Press, Oxford, 2002).

[23] F. Minganti, A. Biella, N. Bartolo, and C. Ciuti, Spectral theory of liouvillians for dissipative phase transitions, Phys. Rev. A **98**, 042118 (2018).

[24] B. Kraus, H. P. Büchler, S. Diehl, A. Kantian, A. Micheli, and P. Zoller, Preparation of entangled states by quantum markov processes, Phys. Rev. A **78**, 042307 (2008).

[25] G. Akemann, M. Kieburg, A. Mielke, and T. Prosen, Universal signature from integrability to chaos in dissipative open quantum systems, Phys. Rev. Lett. **123**, 254101 (2019).

[26] L. Sá, P. Ribeiro, and T. Prosen, Complex spacing ratios: A signature of dissipative quantum chaos, Phys. Rev. X **10**, 021019 (2020).

[27] J. Li, T. Prosen, and A. Chan, Spectral statistics of non-hermitian matrices and dissipative quantum chaos, Phys. Rev. Lett. **127**, 170602 (2021).

[28] T. Prosen, Third quantization: a general method to solve master equations for quadratic open fermi systems, New J. Phys. **10**, 043026 (2008).

[29] N. Shibata and H. Katsura, Dissipative spin chain as a non-hermitian kitaev ladder, Phys. Rev. B **99**, 174303 (2019).

[30] M. V. Medvedyeva, F. H. L. Essler, and T. Prosen, Exact bethe ansatz spectrum of a tight-binding chain with dephasing noise, Phys. Rev. Lett. **117**, 137202 (2016).

[31] X.-D. Dai, F. Song, and Z. Wang, Solvable bcs-hubbard liouvillians in arbitrary dimensions, Phys. Rev. B **108**, 115127 (2023).

[32] H. Weimer, A. Kshetrimayum, and R. Orús, Simulation methods for open quantum many-body systems, Rev. Mod. Phys. **93**, 015008 (2021).

[33] G. Chen, F. Song, and J. L. Lado, Topological spin excitations in non-hermitian spin chains with a generalized kernel polynomial algorithm, Phys. Rev. Lett. **130**, 100401 (2023).

[34] The source codes are available on https://github.com/GUANGZECHEN/NHKPM.jl.

[35] A. Weiße, G. Wellein, A. Alvermann, and H. Fehske, The kernel polynomial method, Rev. Mod. Phys. **78**, 275 (2006).

[36] F. A. Wolf, I. P. McCulloch, O. Parcollet, and U. Schollwöck, Chebyshev matrix product state impurity solver for dynamical mean-field theory, Phys. Rev. B **90**, 115124 (2014).

[37] J. L. Lado and O. Zilberberg, Topological spin excitations in harper-heisenberg spin chains, Phys. Rev. Res. **1**, 033009 (2019).

[38] M. Zwolak and G. Vidal, Mixed-state dynamics in one-dimensional quantum lattice systems: A time-dependent super-operator renormalization algorithm, Phys. Rev. Lett. **93**, 207205 (2004).

[39] G. H. Wannier, Dynamics of band electrons in electric and magnetic fields, Rev. Mod. Phys. **34**, 645 (1962).

[40] M. Schulz, C. A. Hooley, R. Moessner, and F. Pollmann, Stark many-body localization, Phys. Rev. Lett. **122**, 040606 (2019).

[41] W. Morong, F. Liu, P. Becker, K. Collins, L. Feng, A. Kyprianidis, G. Pagano, T. You, A. Gorshkov, and C. Monroe, Observation of stark many-body localization without disorder, Nature (London) **599**, 393 (2021).

[42] E. van Nieuwenburg, Y. Baum, and G. Refael, From bloch oscillations to many-body localization in clean interacting systems, Proc. Natl. Acad. Sci. USA **116**, 9269 (2019).

[43] J. Li, T. Wang, L. Luo, S. Vemuri, and Y. N. Joglekar, Unification of quantum zeno–anti zeno effects and parity-time symmetry breaking transitions, Phys. Rev. Res. **5**, 023204 (2023).

[44] A. Teretenkov and O. Lychkovskiy, Exact dynamics of quantum dissipative xx models: Wannier-stark localization in the fragmented operator space, Phys. Rev. B **109**, L140302 (2024).

[45] T. Barthel and Y. Zhang, Solving quasi-free and quadratic lindblad master equations for open fermionic and bosonic systems, J. Stat. Mech.: Theory Exp. (2022) 113101.

[46] H. Pichler, A. J. Daley, and P. Zoller, Nonequilibrium dynamics of bosonic atoms in optical lattices: Decoherence of many-body states due to spontaneous emission, Phys. Rev. A **82**, 063605 (2010).

[47] J. Preskill, Lecture notes for ph219/cs219: Quantum information Chapter 3, California Institute of Technology, 2018.

[48] The dynamical correlator for the steady state being other superposition of $\rho_\pm$ can be obtained via additionally computing $\tilde{C}(t) = \text{tr}(\sigma_N^z e^{t\mathcal{L}}[\sigma_N^z Q])$, for which our method is still workable since Q is also a low-entangled state after the same vectorization as Eq. (4).

[49] L.-N. Wu and A. Eckardt, Bath-induced decay of stark many-body localization, Phys. Rev. Lett. **123**, 030602 (2019).

[50] R. Ghosh and M. Žnidarič, Relaxation of imbalance in a disordered xx model with on-site dephasing, Phys. Rev. B **107**, 184303 (2023).

[51] K. Kawabata, R. Sohal, and S. Ryu, Lieb-schultz-mattis theorem in open quantum systems, Phys. Rev. Lett. **132**, 070402 (2024).

[52] G. Vidal, Efficient classical simulation of slightly entangled quantum computations, Phys. Rev. Lett. **91**, 147902 (2003).

[53] E. Wybo, M. Knap, and F. Pollmann, Entanglement dynamics of a many-body localized system coupled to a bath, Phys. Rev. B **102**, 064304 (2020).

[54] J. Haegeman, J. I. Cirac, T. J. Osborne, I. Pižorn, H. Verschelde, and F. Verstraete, Time-dependent variational principle for quantum lattices, Phys. Rev. Lett. **107**, 070601 (2011).

[55] J. Haegeman, C. Lubich, I. Oseledets, B. Vandereycken, and F. Verstraete, Unifying time evolution and optimization with matrix product states, Phys. Rev. B **94**, 165116 (2016).

[56] S. E. Begg and R. Hanai, Quantum criticality in open quantum spin chains with nonreciprocity, Phys. Rev. Lett. **132**, 120401 (2024).

[57] K. Yamamoto, M. Nakagawa, M. Tezuka, M. Ueda, and N. Kawakami, Universal properties of dissipative tomonaga-luttinger liquids: Case study of a non-hermitian xxz spin chain, Phys. Rev. B **105**, 205125 (2022).

[58] T. Prosen, Exact nonequilibrium steady state of a strongly driven open *xxz* chain, Phys. Rev. Lett. **107**, 137201 (2011).

[59] T. Prosen, Exact nonequilibrium steady state of an open hubbard chain, Phys. Rev. Lett. **112**, 030603 (2014).

[60] K. Li and Y. Xu, Non-hermitian absorption spectroscopy, Phys. Rev. Lett. **129**, 093001 (2022).

[61] M.-M. Cao, K. Li, W.-D. Zhao, W.-X. Guo, B.-X. Qi, X.-Y. Chang, Z.-C. Zhou, Y. Xu, and L.-M. Duan, Probing complex-energy topology via non-hermitian absorption spectroscopy in a trapped ion simulator, Phys. Rev. Lett. **130**, 163001 (2023).

[62] M. Fishman, S. R. White, and E. M. Stoudenmire, The ITensor software library for tensor network calculations, SciPost Phys. Codebases **4**, 1 (2022).

[63] H. G. Dawson, On the numerical value of $\int_0^h \exp(x^2)dx$, Proc. Lond. Math. Soc. **s1-29**, 519 (1897).

[64] C. Runge, Ueber die numerische auflösung von differentialgleichungen, Math. Ann. **46**, 167 (1895).

[65] P. Jordan and E. Wigner, Über das paulische Äquivalenzverbot, Zeitschrift för Physik **47**, 631 (1928).